New Journal of Physics
The open access journal at the forefront of physics

Deutsche Physikalische Gesellschaft DPG IOP Institute of Physics

PAPER • OPEN ACCESS

Evaluation of similarities and differences of $LiTaO_3$ and $LiNbO_3$ based on high-*T*-conductivity, nonlinear optical fs-spectroscopy and *ab initio* modeling of polaronic structures

To cite this article: A Krampf *et al* 2021 *New J. Phys.* **23** 033016

New Journal of Physics
The open access journal at the forefront of physics

Deutsche Physikalische Gesellschaft DPG
IOP Institute of Physics

Published in partnership with: Deutsche Physikalische Gesellschaft and the Institute of Physics

OPEN ACCESS

RECEIVED
26 September 2020

REVISED
18 January 2021

ACCEPTED FOR PUBLICATION
5 February 2021

PUBLISHED
15 March 2021

PAPER

Evaluation of similarities and differences of $LiTaO_3$ and $LiNbO_3$ based on high-*T*-conductivity, nonlinear optical fs-spectroscopy and *ab initio* modeling of polaronic structures

A Krampf[1], M Imlau[1], Y Suhak[2], H Fritze[2] and S Sanna[3,*]

[1] School of Physics, University of Osnabrueck, Barbarastrasse 7, 49076 Osnabrueck, Germany
[2] Institut für Energieforschung und Physikalische Technologien, Technische Universität Clausthal, Am Stollen 19B, 38640 Goslar, Germany
[3] Institut für Theoretische Physik and Center for Materials Research (LaMa), Justus-Liebig-Universität Gießen, 35392 Gießen, Germany
[*] Author to whom any correspondence should be addressed.

E-mail: simone.sanna@theo.physik.uni-giessen.de

Keywords: small polarons, self-trapped excitons, unltrafst nonlinear optical spectroscopy, ferroelectrics, DFT, electric conductivity, atomistic simulations

Abstract

Different aspects of ferroelectric $LiTaO_3$ (LT) such as polaronic defects, optical response and electrical conductivity are investigated by the most recent theoretical and experimental approaches. Comparing the results with the state-of-the-art knowledge of the widely studied $LiNbO_3$ (LN), we evaluate the general assumption that there is little difference between the aforementioned properties of LT and LN. First-principles calculations reveal the existence of point defects in LT qualitatively compatible with the polaronic picture established in LN. Though, peculiar differences with respect to the individual binding energies and polaronic deformation can be revealed. Accordingly, (sub-)picosecond transient absorption measurements show pronounced differences in the kinetics in the sub-ps time domain of small polaron formation and, even more pronounced, in the long-term evolution identified with small polaron hopping. In contrast, (sub-)ps transient luminescence, attributed to the relaxation of self-trapped excitons in LN, shows very similar kinetics. Electrical conductivity measurements are performed in air as function of temperature. Up to about 600 °C they demonstrate similar temperature dependence for the two materials, from which rather comparable activation energies can be extracted. However, in the high-temperature range from about 600 °C to 920 °C both materials show noticeable differences. The results suggest that the fundamental microscopic understanding of LN can be in part transferred to LT. However, due to differences in structure, energetic landscape and temperature behavior, discrepancies between the two materials bear a striking potential for novel applications, even at high temperatures.

1. Introduction

Since the discovery of its ferroelectric nature in 1949 [1], $LiNbO_3$ (LN) has become one of the most employed electro-acoustic and electro-optical materials for technological applications. Its uncommon, unusually large and favorable properties [2, 3] are indeed exploited in a wealth of applications. Correspondingly, $LiNbO_3$ is one of the most intensively investigated ferroelectrics [4–15]. The effort of the ferroelectric community, in particular in the last 50 years, has led to unprecedent deep insight in the physical mechanisms determining the materials characteristics. A row of material properties, including its optical response, can be interpreted and modeled within the concept of quasiparticles called polarons and their dynamics [16]. Furthermore, $LiNbO_3$ has become a testbed for generations of scientists, trying to tailor its optical properties or elucidate and enhance technologically relevant effects (e.g. the bulk photovoltaic effect [17]). Many of the material's properties are largely determined by intrinsic defects

[18, 19], which are present in high concentrations due to the Li-deficient growth (congruent composition). Structural models based on Nb vacancies [20] or Li vacancies [21, 22] have been proposed by different scientists to explain the congruent composition. Vibrational spectroscopy has provided valuable information concerning the material composition [4, 5, 11–13, 23, 24]. Summarizing, $LiNbO_3$ has been the drosophila of the optically active ferroelectrics, on which a wealth of ideas, technologies and procedures have been tested [25–28]. In addition, high-temperature properties are attracting increasing interest, since the piezoelectric coefficients of LN are very high compared to high-temperature stable piezoelectric crystals such as langasite ($La_3Ga_5SiO_{14}$ [29, 30]), and thus $LiNbO_3$ based actuator applications are desired. Related investigations of the thermal stability and of the atomistic transport processes has been performed as function of Li content [31–33].

At the same time, our knowledge of similar ferroelectric crystals such as ferroelectric $LiTaO_3$ is rather limited. Lithium tantalate is, like $LiNbO_3$, an opical crystal [34, 35], which is the functional material in devices exploiting its bulk [36, 37] or surface properties. LT crystallizes within the *R*3*c* space group below the Curie temperature as lithium niobate [2, 38, 39], and within the space group $R\bar{3}c$ above it [40, 41]. The lack of a comprehensive literature about LT might be in part due to the common assumption that the properties of structurally and electronically similar ferroelectric crystals such as LN and LT differ only slightly, and a corresponding systematic is not necessary. Also, some of the crystal physical parameters in LT, such as electro-optic coefficient, do not reach the magnitudes found in LN. However, it is also reported that LT features severe fundamental differences to LN, for example the Curie (940 K vs 1480 K) [42] and melting (1923 K vs 1526 K) [43] temperatures, as well as the coercive fields (17 kV cm^{-1} vs 40 kV mm^{-1}) [44] are very different in the two compounds. These aspects are of particular relevance in applications where ferroelectric poling, transport along ferroelectric domain walls, or high-temperature stability are exploited.

In order to evaluate the validity of the general assumption that there is only little difference between LN and LT, we identify at fist the most representative properties of the model system LN. LN is one of the most important opto-electronic materials, with a multitude of further applications in surface acoustic devices and sensors. Therefore polaronic structures, optical response and transport properties are chosen as characteristic and crucial aspects of LN. This list of properties is of course not exhaustive, however it suffices to provide a representative description of the material. In a second step, we perform an independent investigation of the selected properties in LN and LT, using the most advanced methods available to highlight differences and similarities between the two materials.

Commercially available LN samples are strongly Li deficient and their composition is referred to as congruent. Congruent crystals are characterized by a substantial concentration of point defects. Among these, Nb_{Li} antisites are able to localize electrons in their close neighborhood, resulting in the formation of small electron polarons. It might thus be expected that electron polarons also exist in the isomorphic and isoelectronic lithium tantalate, which also crystallizes in a congruent composition. However, the proof of the existence of small polarons in $LiTaO_3$ is still missing. Although vacancies [45] and defect clusters [46] have been investigated from first principles, a detailed theoretical description of polaronic defects in LT elucidating the interplay between atomic and electronic structure is not available in the literature.

In this work, we at first explore the possibility of polaron formation in $LiTaO_3$. The goal is the identification of defect centers compatible with the polaronic picture. We provide an atomistic description of polaronic defects at the microscopic scale based on *ab initio* models within the DFT $+U$ method. This method allows for the accurate modeling of strongly correlated electrons such as the Ta 5*d* orbitals, and is thus essential for an accurate modeling of the investigated materials. Free polarons, for which an atomistic description is missing both in LN and LT, as well as intrinsic bound small polarons or bipolarons are considered. We demonstrate that structural properties, the electronic band structures as well as the spatial extension of the squared wavefunctions of isolated Ta_{Li}^{4+} antisites and nearest-neighbor $Ta_{Li}^{4+} - Ta_{Ta}^{4+}$ pairs are compatible with the polaronic picture. Similarities and differences with corresponding structures in LN are discussed.

In a second step, we perform (sub)picosecond time-resolved absorption and luminescence spectroscopy to investigate the optical response dynamics of congruent LT and LN single crystals. It is already widely accepted, that (ultrafast) absorption spectroscopy is a powerful tool to inspect the formation dynamics on the sub-ps time domain and the hopping and recombination regime that is reported up to milliseconds. In contrast, transient luminescence on the sub-ps to ps-time scale is associated with the relaxation dynamic of self-trapped excitons. The latter is investigated in this study with the recently introduced technique of femtosecond fluorescence upconversion spectroscopy, modified for the inspection of weakly luminescing solid state samples [47]. Accordingly, the results presented here are the first reported for $LiTaO_3$ in the difficult to access (sub)picosecond time range, providing insight into the early stages of carrier localization phenomena. As to be expected from the findings in the energetic landscapes of the polaronic states, the transient absorption reveals significant differences in the sub-ps time-domain of formation kinetics. More

pronounced, we find an increase of the lifetime in the transport hopping regime, while overall kinetics are less manifold. In the transient luminescence, in contrast, on ultrashort timescales both samples show practically identical kinetics. Assuming its origin from optically generated self-trapped excitons as in LN, it can be concluded that the features related to the ideal LT lattice are not very much altered when compared with LN.

Finally, measurements of electrical conductivity are performed in the temperature range from about 350 °C to 920 °C for congruent $LiNbO_3$ and $LiTaO_3$ crystals. Up to 600 °C, the activation energies have similar values. Furthermore, the magnitude of the conductivity of both materials differs only slightly. At 600 °C, Czochralski grown LN and LT exhibit conductivities of 2.6×10^{-4} and 3.0×10^{-4} S m^{-1}, respectively. Consequently, similar transport mechanisms appear to be dominant. However, in the high-temperature range from about 600 °C to 920 °C both materials show noticeable differences. The activation energies cannot yet be determined as the underlying transport mechanisms are currently not clear.

The results of these investigations suggest that although the fundamental microscopic understanding of LN can be transferred to LT, differences in structure, energetic landscape and temperature behavior are present, which bare striking potential for novel applications even at high temperatures.

2. Methods and sample preparation

2.1. Computational approach

The Vienna *ab initio* simulation package VASP [48, 49] is employed to perform first-principles total-energy calculations within the spin-polarized density functional theory. We consider a number of valence electrons equal to 3 per atom for lithium ($1s^2\ 2s^1$), 13 for niobium ($4s^2\ 4p^6\ 4d^3\ 5s^2$), 11 for tantalum ($5p^6\ 5d^3\ 6s^2$), and six for oxygen ($2s^2\ 2p^4$). The projector-augmented wave (PAW) [50, 51] method is employed to account for remaining core electrons. Following the tests performed in reference [52], we chose to employ the semi-local exchange-correlation functional proposed by Perdew, Burke, and Ernzerhof (PBE [53]). We furthermore make use of a plane wave basis containing waves up to a kinetic energy of 400 eV to expand the electronic wave functions. The atomic positions are self consistently optimized until Hellmann–Feynman forces lower than 0.001 eV Å^{-1} are present on each atom. $2 \times 2 \times 2$ k-point meshes generated with the Monkhorst–Pack algorithm [54] and centered to the Γ-point are employed to perform the energy integration in the Brillouin zone. Convergence tests show that within this approach leads to converged results concerning total energies and forces.

Isolated free and bound polarons are modeled with rhombohedral cells of 2853.68 Å^3 for LT and 2869.59 Å^3 for LN containing 270 atoms. The correct treatment of the d orbitals of Ta and Nb is typically problematic in DFT due to the strong electronic correlation. The strong on-site Coulomb repulsion of such electrons is accounted for in this work by the approach commonly referred to as the DFT $+U$ method. Within this method, a strong intra-atomic interaction is introducted in a (screened) Hartree–Fock like manner, as an on-site replacement of the L(S)DA [55]. In the present investigation, we apply the simplified approach proposed by Dudarev *et al* [56]. The rotationally invariant DFT $+U$ functional is thereby described by

$$E = E_{\mathrm{LDA}} - \frac{1}{2}UN(N-1) + \frac{1}{2}U\sum_{i\neq j} n_i n_j. \tag{1}$$

The indices i and j run over all the electronic levels of the Ta 5d or Nb 4d orbitals. U is the spherical averaged Hubbard correction, which models the enhanced Coulomb interaction. The eigenstates ε_i are then calculated as the derivatives of equation (1) with respect to the occupation numbers n_i:

$$\varepsilon_i = \frac{\partial E}{\partial n_i} = \varepsilon_{\mathrm{LDA}} + U\left(\frac{1}{2} - n_i\right). \tag{2}$$

As a consequence of the Hubbard correction, the lower Hubbard subband (occupied d orbitals) is shifted downwards, while the upper Hubbard subband is shifted to higher energies [58]. In the approach applied in this work the shift is proportional to the difference $U' = U - J$, which can be interpreted as an effective U. J, an approximation of the Stoner exchange parameter, is the screened exchange energy, which is roughly equal to 1 eV [59]. According to the tests performed in reference [42, 60, 61], we chose $U' = 4$ eV for LN and $U' = 5$ eV for LT. Different values shift the position of the localized defect states within the band gap, without qualitatively modifying the behavior of the polaronic defects. This approach has led to the reliable description of intrinsic and extrinsic polarons in $LiNbO_3$ [62–64].

2.2. Picosecond transient absorption and luminescence

Transient absorption kinetics is studied using a conventional, home-built pump-probe-technique based on a regeneratively amplified Ti-sapphire laser and an optical parametric amplifier (OPA) as described in reference [47]. Both samples are excited at a repetition rate of 1 kHz using intense, frequency-doubled fs-laser pulses ($\lambda = 400$ nm, $\tau = 60$ fs, $E = 65$ μJ). The OPA is tuned to generate probe pulses in the near-infrared spectral range ($\lambda = 910$ nm). The transmitted probe pulse for a specific temporal delay between the pump and probe pulse is recorded and analyzed with a thermoelectrically-cooled 2D-CCD-array attached to a Czerny–Turner monochromator. The detected spectra are spectrally integrated to obtain a signal I proportional to the transmitted pulse energy. For each temporal delay, the absorbance is calculated via

$$A(t) = -\log\left(I(t)/I(t \ll 0)\right), \tag{3}$$

where $I(t \ll 0)$ is the spectrally integrated pulse signal for time delays at which the probe pulse arrives at the sample before excitation. The apparatus response function has a full width at half maximum of $\approx$130 fs.

Transient luminescence on the (sub-)ps-timescale is investigated applying broadband fs-fluorescence upconversion spectroscopy [65] adapted to the inspection of single crystals in reflection geometry (for a detailed description of the experimental setup see reference [47]). The same fs laser pulses as in the absorption measurement are used to excite the samples. The emitted luminescence is collected with an off-axis Cassegrain reflector and imaged onto a BBO crystal. There it is superposed with intense, tilted and compressed fs-laser pulses ($\lambda = 1340$ nm, $\tau = 45$ fs, $E = 50$ μJ) provided by the OPA for non-collinear sum-frequency mixing. For fixed time delays, the generated sum-frequency spectra are again recorded with the monochromator-CCD-detection system. The Gaussian-shaped apparatus response function of this experimental setup has a full width at half maximum of $\leqslant$160 fs.

Experimental techniques providing highest temporal resolutions are powerful tools for the study of charge-carriers and excitons with strong lattice coupling in ABO_3 perovskite-like ferroelectrics, as the formation of these transients in such materials is extraordinarily fast ($\leqslant$300 fs [47, 66–68]). Photoluminescence spectroscopy is of special importance where the absorption feature of a transient is experimentally inaccessible, however it has been seldom applied to ABO_3 ferroelectric solids [47]. To the best of our knowledge, the transient absorption and the photoluminescence features of $LiTaO_3$ with a sub-picosecond temporal resolution were not investigated so far.

2.3. Conductivity measurements

The electrical conductivity of $LiNbO_3$ and $LiTaO_3$ single crystals is determined by AC impedance spectroscopy in the frequency range from 1 Hz to 1 MHz using an impedance/gain-phase analyzer (Solartron 1260). The measurements are performed in a tube furnace that allows heating up to 1000 °C in air at atmospheric pressure while heating at a rate of 1 K min^{-1} from room temperature (RT).

An electrical equivalent-circuit model consisting of a constant phase element (CPE) connected in parallel with a bulk resistance R_B is fitted to measured data. The bulk conductivity σ is subsequently calculated from the relation $\sigma = t(AR_B)^{-1}$, where t and A are the thickness of the sample and the electrode area, respectively. Further, the activation energy E_A is extracted from the Arrhenius relation

$$\sigma = \sigma_0/T \exp\left(-E_A/(k_B T)\right), \tag{4}$$

where σ_0, k_B and T are a constant pre-exponential coefficient, the Boltzmann constant, and the absolute temperature, respectively.

The activation energy E_A can be extracted from equation (4) provided that a single conduction mechanism dominates in a sufficiently large temperature range. This fact is reflected by a constant slope in the Arrhenius representation that can be attributed to E_A. The slope used here is denoted by $E_{\sigma T}$ and follows from

$$E_{\sigma T} = -k_B \frac{\partial \ln(\sigma T)}{\partial(1/T)}. \tag{5}$$

The consideration of σT is motivated in section 3.3.

2.4. Crystal growth and sample preparation

Optical measurements are conducted on rectangular plates of congruent lithium niobate ($9 \times 10 \times 0.2$ mm^3, X-cut) and lithium tantalate ($7 \times 8 \times 0.5$ mm^3, Z-cut) grown by the Czochralski method at the WIGNER Research Center for Physics, Budapest, and at the University of Osnabrueck, respectively. Both samples are cut and polished to optical quality. Transient luminescence and absorption are both detected for ordinary (probe) polarisation.

The crystals for the study of the electrical properties are prepared by the Czochralski method at the Institute of Microelectronics Technology and High Purity Materials, Russian Academy of Sciences, Moscow, and subsequently prepared as polished X-cut rectangular plates with dimensions of $8 \times 20 \times 1.6$ mm^3. Further, Pt-electrodes with a thickness of $\sim$3 μm are deposited by screen printing (print ink: Ferro Corporation, No. 6412 0410). After screen-printing, the specimens are annealed at 1000 °C for about 30 min.

3. Results and discussion

3.1. Polaronic defects

3.1.1. Free polarons

Free small polarons are quasiparticles that are formed in crystals with large lattice polarizability, when the electron (or hole)–lattice interaction is large enough to overcome the Coulomb repulsion and localize the carrier at substantially one lattice site [16]. Electrons self-trapped at the regular Nb^{5+} ($4d^0$) ions of the LN lattice are paradigmatic examples of free small polarons. Although the optical absorption bands caused by free polarons in LN have been measured [16], a quantitative structural model based on atomistic calculations is still missing. This is probably due to the fact that the additional electron is strongly localized and therefore difficult to model within conventional DFT.

The presence of an electron at the regular Nb^{5+} (Ta^{5+}) lattice site affects the crystal morphology in its neighborhood. According to our calculations, the Nb (Ta) ion moves into a more central position within the oxygen octahedron, which expands by 2.20% in LN and 2.39% in LT. The bond distances of the Nb (Ta) ion (at which the free polaron is localized) with the first oxygen neighbors are reported in table 1. Although the magnitude of the lattice expansion is slightly larger in LT than in LN, the corresponding distortion costs elastic energy of ca 500 meV in both materials. This suggests a similar high lattice polarizability for both compounds.

The band structures calculated for a supercell containing the free polaron in LN and LT are shown in figure 1. The defect state related to the self trapped electron is clearly observable and is located 0.65 eV below the conduction band in LN and 0.69 eV in LT. Calculations performed with supercells of different size and extrapolation to infinite supercells suggest the free polaron level at about 0.60 eV below the conduction band for both LN and LT. This is compatible with the onset of the free-polaron related optical absorption as measured in LN [16].

In order to determine how far the self trapped charge carrier is localized at the Ta and Nb lattice site or rather delocalized over several unit cells, we have calculated the charge density difference between a supercells with and without the free polaron. The result of this procedure is shown in figure 2. The electron captured upon 5+/4+ transition is strongly localized at substantially one lattice site, which is typical for small polarons. The squared wavefunctions are rather similar to the Ta or Nb d_{z^2} orbitals building the bulk conduction band.

3.1.2. Bound small polarons

In $LiNbO_3$, an electron is localized at the Nb_{Li}^{5+} ($4d^0$) site by the electron–lattice interaction, which results in a consistent lattice distortion. With respect to the free polarons, the positive potential due to the antisite defect additionally binds the electron. Thus, the charged antisite, Nb_{Li}^{4+} ($4d^1$), is usually addressed to as a bound (small) polaron.

The signatures in the optical spectra of $LiNbO_3$ can be interpreted within the polaronic picture. In the absorption spectra the photoexcited peak at roughly 1.6 eV is assigned to bound small polarons. Furthermore they are involved in different processes determining the material's optical response [16]. It is therefore not surprising, that different research groups have theoretically modeled niobium antisites in $LiNbO_3$ [62, 69–73]. We have simulated differently charged Nb_{Li} antisites with the computational approach described in section 2.1 in order to have a term of comparison for possible polaronic defects (Ta_{Li} antisites) in LT. The polaronic distortion upon single ($Nb_{Li}^{5+} \rightarrow Nb_{Li}^{4+}$) and double ($Nb_{Li}^{5+} \rightarrow Nb_{Li}^{3+}$) electronic capture is pronounced, as shown in table 2. The corresponding electronic structure, with the typical polaron-related electronic state which lowers its energy with increasing occupation, is shown in figures 3(a) and (b). The calculated data closely reproduce small bound polarons in $LiNbO_3$ as described, e.g. by Nahm and Park with a similar approach [62].

A similar, detailed description of tantalum antisites in $LiTaO_3$ is not available, though. Here, we focus on the description of the atomic and electronic structure of bound small polarons in $LiTaO_3$, as calculated with the previously described spin-polarized DFT $+U$ approach.

Table 1. Atomic distances (in Å) in the neighborhood of the regular Nb^{5+} (Ta^{5+}) site in $LiNbO_3$ ($LiTaO_3$) without and with a free polaron. X labels either a Nb or a Ta ion, % indicates the relative expansion of the oxygen octahedron upon free polaron localization.

System	X-O_1	X-O_2	Avg. X-O	%
Nb^{5+}_{Nb}	1.938	2.073	2.006	
Nb^{4+}_{Nb}	2.016	2.084	2.050	2.20
Ta^{5+}_{Ta}	1.975	2.035	2.005	
Ta^{4+}_{Ta}	2.035	2.070	2.053	2.39

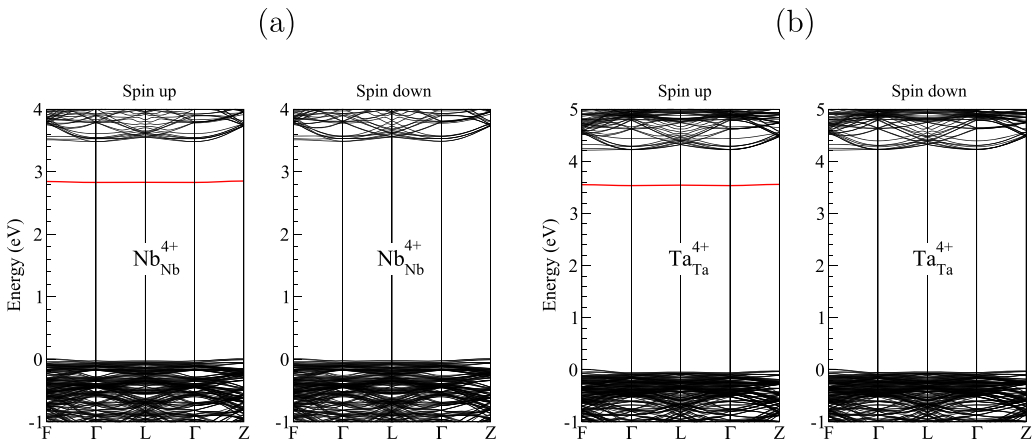

Figure 1. Electronic band structures of the supercells modeling a free polaron in $LiNbO_3$ (a) and $LiTaO_3$ (b). The localized electronic state related to the free polaron is plotted in red (spin up channel). The corresponding empty state in the spin down channel is in the conduction band.

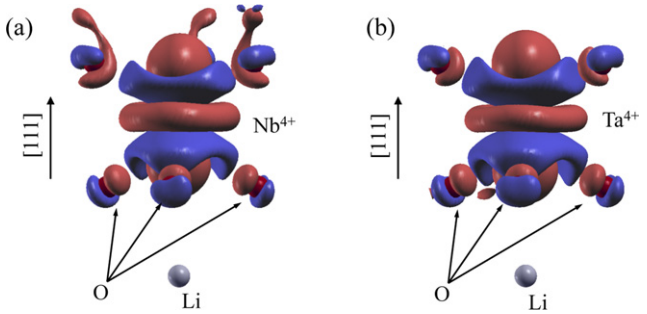

Figure 2. Electronic charge related to the free polaron state in $LiNbO_3$ (a) and $LiTaO_3$ (b). The electronic charge is completely localized around the Nb^{4+}_{Nb} (Ta^{4+}_{Ta}) lattice site. The (red/blue) isosurfaces for (positive/negative) density charges 0.02 e $Å^{-3}$ are shown.

Table 2. Atomic distances (in Å) in the neighborhood of the Li site in $LiNbO_3$. X labels a Li at a regular lattice site or a substitutional Nb. X-Nb labels the distance along the [111] crystallographic direction.

System	X-O_1	X-O_2	Avg. X-O	X-Nb
Li^{+}_{Li}	2.014	2.306	2.160	3.082
Nb^{5+}_{Li}	1.940	2.091	2.015	3.045
Nb^{4+}_{Li}	2.024	2.122	2.073	2.963
$Nb^{4+}_{Li} - Nb^{4+}_{Nb}$	2.066	2.104	2.085	2.661

If a Li is replaced by a Ta atom in $LiTaO_3$, the lattice rearranges locally. As a consequence of the smaller ionic radii of Ta ions with respect to Li (see table 3), the oxygen octaedra around the substitutional is contracted with respect to the ideal lattice, as shown in table 4.

In the charge state 5+ the Ta_{Li} antisite hs the electronic configuration $5d^0$ and is isovalent with the replaced Li^+ ion. The average Ta_{Li}–O distance shrinks from 2.164 Å to 2.023 Å, and a localized defect level

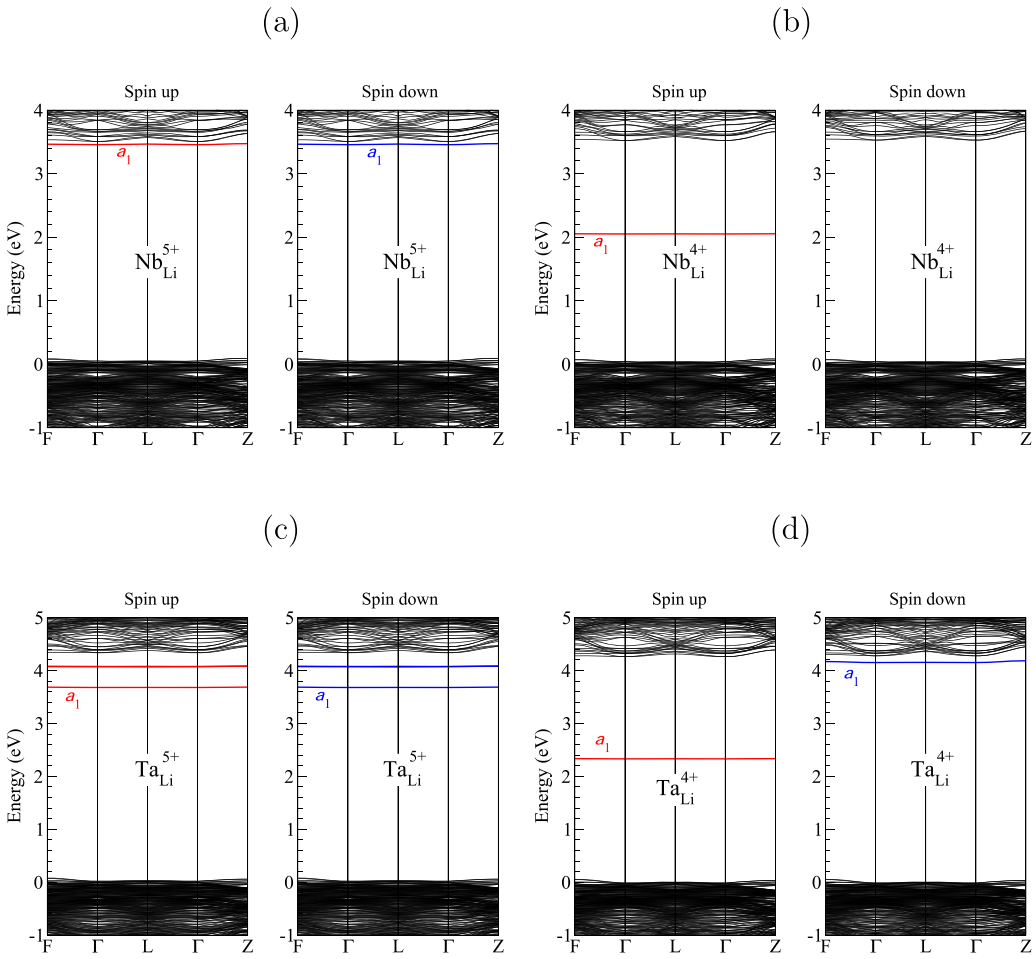

Figure 3. Electronic band structures of the supercells modeling the Nb_{Li}^{5+} and Nb_{Li}^{4+} antisites in $LiNbO_3$ (a) and (b) as well as the Ta_{Li}^{5+} and Ta_{Li}^{4+} antisites in $LiTaO_3$ (c) and (d). Localized defect states are shown in red (spin up) or blue (spin down).

Table 3. Ionic radii (in Å) of the considered species for octahedral coordination. Data from reference [57].

Ion	Li^+	Ta^{5+}	Ta^{4+}	Ta^{3+}	Nb^{5+}	Nb^{4+}	Nb^{3+}
Radius	0.90	0.78	0.82	0.86	0.78	0.82	0.86

Table 4. Atomic distances (in Å) in the neighborhood of the Li site in $LiTaO_3$. X labels a Li at a regular lattice site or a substitutional Ta. X-Ta labels the distance along the [111] crystallographic direction.

System	X-O_1	X-O_2	Avg. X-O	X-Ta
Li_{Li}^{+}	1.971	2.358	2.164	2.997
Ta_{Li}^{5+}	1.958	2.087	2.023	3.015
Ta_{Li}^{4+}	2.028	2.136	2.082	2.908
$Ta_{Li}^{4+} - Ta_{Ta}^{4+}$	2.069	2.123	2.096	2.646

is formed very close to the conduction band edge (blue and red bands in figure 3(c)). This electronic level can accommodate up to two electrons. If an electron is localized at the Ta_{Li} defect, the shallow state in the spin-up channel becomes a mid-gap level (see figure 3(d)), while the corresponding empty state in the spin-down channel is within the conduction band. This behavior is unexpected, as Coulomb repulsion should shift upwards upon occupation. However, the energy release due to the lattice relaxation stabilizes the system. The average Ta_{Li}–O interatomic distance grows from 2.023 Å to 2.082 Å due to the Coulomb repulsion as a consequence of the electron localization. This is similar in magnitude to the behavior of the Nb_{Li} antisite in LN and is typical for a polaronic system. Similarly to LN, antisite-induced flat electronic states are present in proximity of the conduction band in LT. Upon electronic capture these levels are

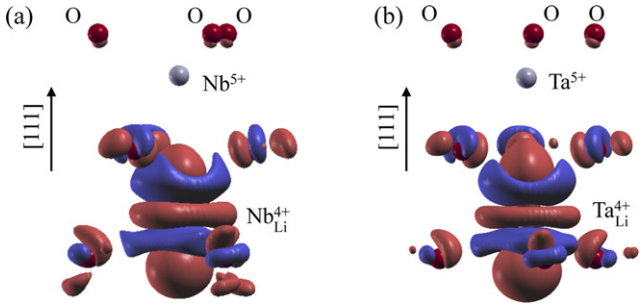

Figure 4. Electronic charge associated with the bound polaron state in LN (a) and LT (b). The electron captured upon Nb^{5+}/Nb^{4+} (or Ta^{5+}/Ta^{4+}) transition is strongly localized in the neighborhood of the antisite. The (red/blue) isosurfaces for (positive/negative) density charges 0.02 e $Å^{-3}$ are shown.

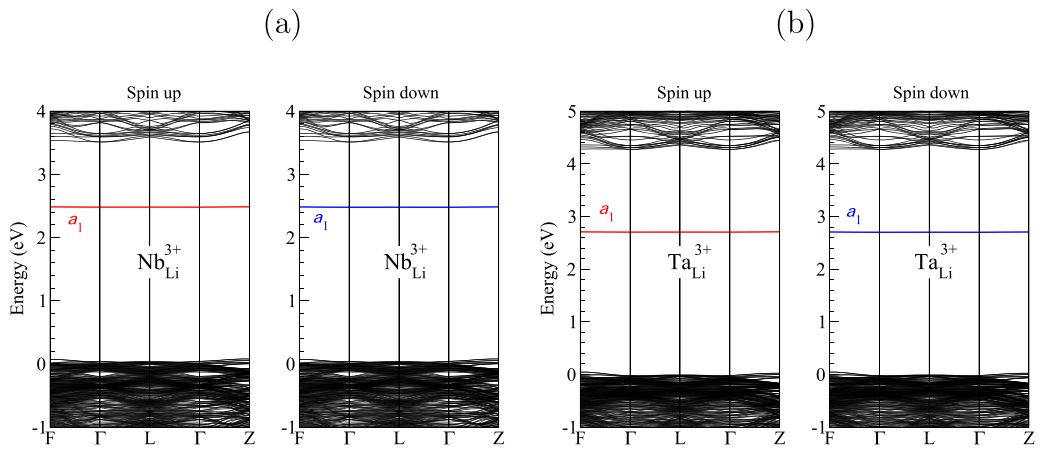

Figure 5. Electronic band structure of the supercells modeling the Nb_{Li}^{3+} antisite in $LiNbO_3$ (a) and the Ta_{Li}^{3+} antisite in $LiTaO_3$ (b). Defect related electronic states are displayed in red (spin up) or blue (spin down).

stabilized by the concomitant structural relaxation. The lattice distortion associated with the bound polaron formation is energetically more expensive in LT (715 meV) than in LN (663 meV).

To give an estimate of the wavefunction localization in bound polarons in $LiTaO_3$, we plot the charge density difference of the antisite in the two configurations Ta_{Li}^{4+} ($5d^1$) and Ta_{Li}^{5+} ($5d^0$) in figure 4. Similarly to free polarons in the same system, the squared wavefunctions are strongly localized in the neighborhood of the antisite, which is the hallmark of small polarons. The strong resemblance with the atomic Ta d_{z^2} states suggests a minor hybridization of these orbitals.

3.1.3. Bipolarons

The capture of a second electron at a Nb_{Li} antisite in $LiNbO_3$ leads to the formation of a nearest-neighbor pair $Nb_{Li}^{4+} - Nb_{Nb}^{4+}$ ($4d^1 - 4d^1$). The pair is stabilized by the formation of a new bond along the *z*-axis. Accordingly, the distance between the involved atoms is strongly reduced (see table 2). The described defect pair is commonly accepted as model for bound bipolarons.

In $LiTaO_3$, when a second electron is hosted in the defect level represented in figure 3(d), the system experienced a deep modification of the electronic and atomic structure. The corresponding electronic structure is displayed in figure 5(b). In case of double occupation, the Ta_{Li} antisite and the nearest-neighbor Ta_{Ta} move toward each other along the [111] crystallographic axis by 0.240 Å. This major lattice relaxation is clearly explained by the electronic charge distribution. The difference between the Ta_{Li}^{3+} antisite (nominal electronic configuration $5d^2$) and the Ta_{Li}^{4+} antisite (electronic configuration $5d^1$) is plotted in figure 6(b). The squared wavefunction does not only surround the antisite as in the case of small bound polarons, but reaches the nearest-neighbor Ta at a regular Ta lattice site. Similarly to the Nb_{Li}-antisites in LN, new bond is created by the hybridization of an antisite electronic state with a 5*d* orbital of the Ta_{Ta}. The system is thus stabilized by the formation of a covalent bond. More important, the charge distribution suggests that the system is more appropriately described as a nearest-neighbor pair $Ta_{Li}^{4+} - Ta_{Ta}^{4+}$ ($5d^1 - 5d^1$) than as a Ta_{Li}^{3+} ($5d^2$) defect. The doubly charged antisites are thus compatible with our knowledge of bipolarons, that consist of coupled free polarons and small bound polarons. Again, the microscopic description of

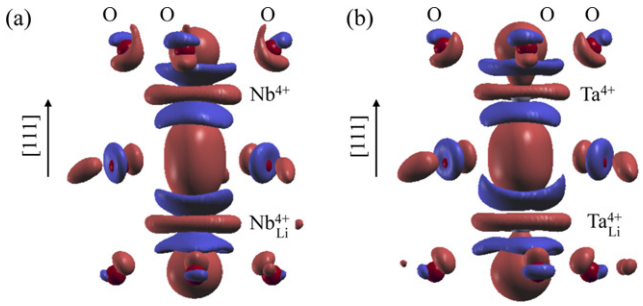

Figure 6. Electronic charge related to the bipolaron in LN (a) and LT (b). The electron captured upon Nb^{4+}/Nb^{3+} (Ta^{4+}/Ta^{3+}) transition is confined at the Nb_{Nb}–Nb_{Li} (Ta_{Ta}–Ta_{Li}) bond formed between the two axial nearest neighbors. The (red/blue) isosurfaces for (positive/negative) density charges ±0.02 e $Å^{-3}$ are shown.

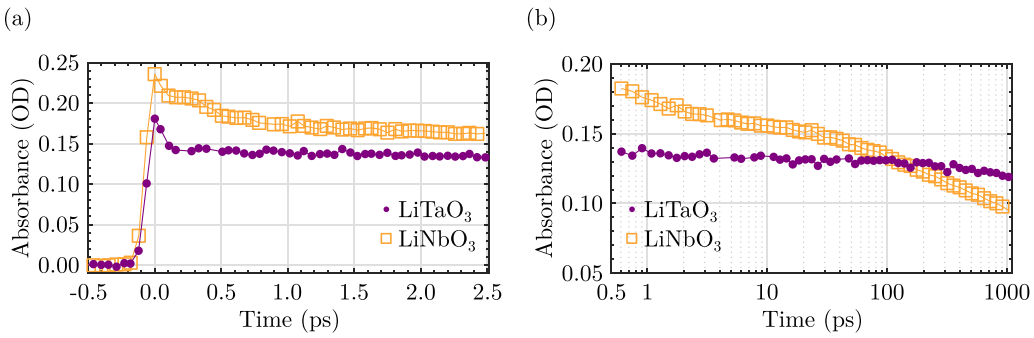

Figure 7. Transient absorbance of LT (violet dots) and LN (yellow squares) measured at a probe wavelength of 910 nm for times (a) up to 2.5 ps and (b) up to 1000 ps.

bipolarons in $LiTaO_3$ strongly resembles its counterpart in $LiNbO_3$. This is illustrated for comparison in table 2 as well as in figures 5(a) and 6(a).

Concluding, we point out that we have demonstrated in previous studies that the Nb_{Li}^{5+} antisite in LN is a so called negative-*U* system, for which a double charge transition is energetically favored [70]. This appears to be in good agreement with the optical studies demonstrating that the bound small polaron Nb_{Li}^{4+} is a metastable state. Small polarons are created by illumination and have a lifetime of about of 10^{-3} seconds [16]. On the other hand, bipolarons are stable systems, which have been assumed both in chemically reduced LN [16] and LT [16, 74], even if they can be dissociated both optically and thermally. Bipolarons are associated to the broad peak in absorption spectra at 2.5 eV in chemically reduced LN and LT [16].

Summarizing, the calculations reveal that the behavior of Ta_{Li} antisites in $LiTaO_3$ and Nb_{Li} antisites in $LiNbO_3$ is similar and typical of polaronic defects. This large family of lattice-carrier quasiparticles is thus not the exclusive hallmark of lithium niobate but also exist in other ionic oxide crystals. However, although polarons in LN and LT are at a first sight identical, differences in binding energies and electronic structures lead to different absorption spectra. Furthermore, as the polaron binding energy is related to the activation energy in transport processes [16], different transport mechanisms might characterize LN and LT.

3.2. Optical response

3.2.1. Transient absorption

The transient absorbance of LT and LN after fs-pulse excitation probed at a wavelength of 910 nm is shown in figure 7. Both kinetics exhibit a steep increase with a small intermediate maximum, which is usually assigned to two-photon absorption of a pump and probe photon [75]. It is therefore used to define time zero. For the congruent LN sample a clear two step decay of the transient absorbance is observed. While the first one has a decay constant of ≈0.7 ps, the second one appears on the picosecond time scale and may correspond to the faster decay observable in the data published by Beyer *et al* [76]. The slower decay can be assigned to absorption of hopping bound polarons [16, 67, 76].

Probing the transient absorption of LT at the same wavelength shows a similarly fast increasing signal but a very different longtime behavior. In contrast to the congruent LN sample a rather constant signal is observed for almost 100 ps followed by a very slow decrease. Surprisingly, the transient absorbance of

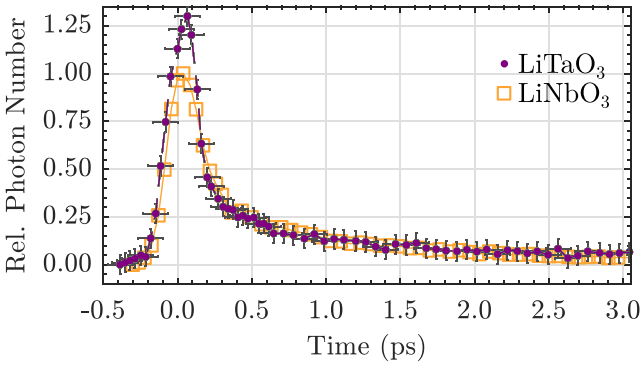

Figure 8. Normalized kinetic traces of the spectrally integrated transient luminescence of LT (violet dots) and LN (yellow squares) single crystals for times up to 3 ps. Data for the LN sample are taken from reference [47].

congruent LT resembles the signal observed in heavily Mg-doped lithium niobate [47]. A clear assignment of the observed transient absorption to antisite bound small polarons is therefore not possible. However, based on the calculations presented here, it is not surprising that antisite bound small polaron hopping in LT and LN is not identical.

In both samples, the transients are generated within a few tens of fs, which is in accordance with small polaron formation observed in LN [66–68]. The rise time of the transient absorption upon the laser pulse is commonly attributed to the time necessary for thermal cooling of hot carriers and the reorganization of the regular lattice. A lower bound for the latter process is mainly determined by the phonon frequency that is reported in the order of 0.1–1 THz in polar oxide crystals [16]. This corresponds to the determined rise time of the transient signals for LT and LN of $\leqslant$100 fs (see figure 7).

Novel model approaches of upcoming studies thus can be easily validated in two different systems. Moreover, taking $LiNb_{1-x}Ta_xO_3$ solid solutions into account, the role of intrinsic disorder and/or defect structure for carrier localization phenomena can be studied in its very detail and may be of major importance for applications at room and/or elevated temperatures.

3.2.2. Transient luminescence

After fs-pulse excitation, both LT and LN show a weak but broad photoluminescence in the blue-green spectral range [77]. Within the error of the experiment, broadband fluorescence upconversion spectroscopy performed in this study and in reference [47] indicates no temporal-stokes shift within the lifetime of the luminescence signal. The spectra are thus integrated to increase the signal-to-noise ratio leading to the kinetic traces shown in figure 8. For both samples, a steep increasing luminescence signal is observed around time zero followed by an equally fast first decay. The latter can be described with an exponential function having a decay time of $\approx$100 fs. Subsequently, the luminescence signal decays exponentially on a picosecond timescale ($\tau = 1$ ps). Within the error of the experiment and except for the peak intensity around time zero, both kinetic traces are practically identical. The luminescence peak around time zero seems to increase with longer illumination times and may thus be related with pump light scattered by an increasingly degraded surface.

The experimental study of the sub-ps kinetics of photoluminescence is a comparably new technique for the inspection of carrier localization phenomena. Based on early findings of Blasse *et al* [78] and the recent systematic studies of Messerschmitdt *et al* [79], Krampf *et al* [47], and Corradi *et al* [80], the RT luminescence may be assigned to the presence of self-trapped excitons bound to the regular Nb–O octahedra in LN. Though the underlying physics still is under investigation, a clear relation to the lattice dynamics is out of question and thus is used as additional fingerprint in the present study.

It is interesting to verify the presence of a sub-ps luminescence in LT crystals, as well, for two reasons: (i) to best of our knowledge it is the very first observation of a room-temperature luminescence kinetics in LT crystals and (ii) it validates the similarities of the (nonlinear) optical responses of the regular LN and LT lattice upon single sub-ps pulse exposure. In particular, the very high consistency in the temporal evolution of the luminescence on a timescale up to 5 ps is remarkable.

As excitons with strong lattice interaction located at Nb–O- and Ta–O-octahedra share a common electronic structure [81–83], we assume the same microscopic processes in LN and LT. In both cases, the transients are formed on a timescale $\leqslant$200 fs which is comparable to the formation time of small polarons in LN estimated to be in the range between 1.5 fs and 300 fs [66–68].

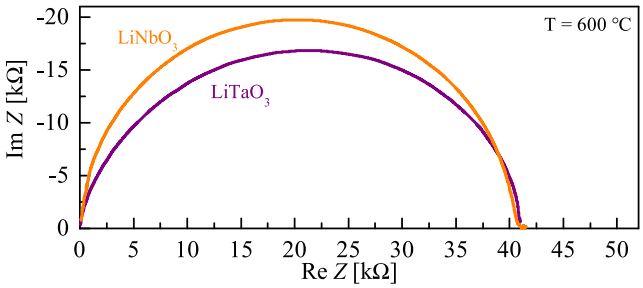

Figure 9. Complex impedance of $LiNbO_3$ and $LiTaO_3$ at 600 °C, presented in form of Nyquist plots.

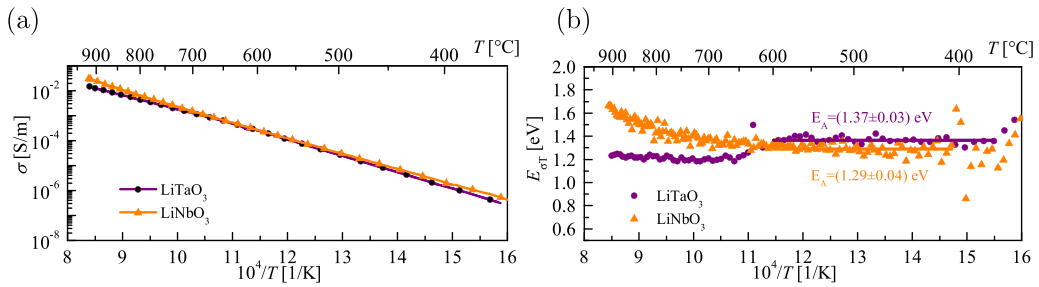

Figure 10. Temperature dependent electrical conductivity of $LiNbO_3$ and $LiTaO_3$ from about 350 °C to 920 °C in ambient air (a) and related slopes $E_{\sigma T}$ (symbols) and activation energies E_A (lines) (b).

3.3. Electrical conductivity

The electrical conductivity is obtained from complex impedance spectra as described in section 2.3. Thereby, the low frequency intercepts of R_B-CPE semicircles in the complex impedance plane are interpreted as bulk resistance and subsequently converted in the bulk conductivity. A Nyquist plot, showing the data in the complex plane, is exemplary given in figure 9 for both studied crystals at 600 °C. As seen from the figure, slightly depressed semicircles with almost similar resistance are obtained. Thereby, it must be noted that

(a) Both specimens in the current study have identical geometries and electrodes and
(b) The slight depression of the semicircles is not relevant for the further discussion. It results from non-ideal capacitances and corresponds to exponents of the CPEs of 0.98 and 0.87 for $LiNbO_3$ and $LiTaO_3$ respectively.

Figure 10(a) shows the temperature dependent electrical conductivity of LN and LT measured in air in the temperature range from about 350 °C to 920 °C in form of an Arrhenius plot. Below about 350 °C the resistivity of both $LiNbO_3$ and $LiTaO_3$ samples is extremely high which does not allow for acquiring reliable data using the setup mentioned in section 2.3. For the sake of clarity, only every fifth and third data point is shown for LN and LT, respectively.

As seen from the figure, both samples exhibit similar electrical conductivities. A slightly different slope is observed, which needs to be evaluated in detail. Figure 10(b) shows the related slopes $E_{\sigma T}$ in the temperature range from about 350 °C to 920 °C.

Below about 600 °C the slopes are constant for both materials. The behavior indicates that the conductivity is governed by a single thermally activated process. Therefore activation energies can be assigned which are $E_A = 1.29 \pm 0.04$ and 1.37 ± 0.03 eV for LN and LT, respectively. In case of LN, the evaluation, i.e. averaging of the slope, is carried out above 405 °C, since the slopes scatter below. However, it can be assumed that E_A is constant down to at least 370 °C. At the latter temperature the evaluation for LT is started. Earlier, it has been shown in reference [84] that the electrical conductivity of congruent LT shows an activation energy of 1.19 ± 0.05 eV in the temperature range from 350 °C to 800 °C. For congruent LN an activation energy of 1.31 eV is found above about 500 °C [32]. The authors conclude that the conductivity is governed by mobile lithium ion vacancies. Similarly to $LiTaO_3$, our previous studies [31, 32] show that the lithium ion migration via lithium vacancies is the dominating transport mechanism in $LiNbO_3$. Accordingly, the product σT must be used to determine the activation energy [84]. Due to the strong similarity of the conductivity as measured in this work for LN and LT, it is plausible to assume that

also in LT the lithium ion migration via lithium vacancies plays a major role below about 600 °C. Indeed, the *ab initio* calculations predict the spontaneous formation of Li vacancies, which are exotherm for a wide range of Fermi energy values within the LT fundamental gap [45].

Above 600 °C the behavior differs. LT shows a slightly decreased slope $E_{\sigma T}$ with respect to the situation below 600 °C. Moreover, the slope is constant. In contrast, the slope for LN increases gradually with increasing temperature which indicates a transition range with contributions of two or more conduction mechanisms. The increasing activation energy is consistent with data from [31] showing an activation energy of 1.37 ± 0.01 eV at 700 °C. However, for our data, the activation energy cannot be determined. In case of LN the slope is not constant whereas in LT the underlying conductivity mechanism is not known. As a consequence it is not clear for LN whether the activation energy must be determined for σT or σ. The essential and most obvious result is that the electrical conductivity of LN and LT differ noticeably above 600 °C.

At this point, we want to emphasize that the correlation of the defect structure and the high-temperature transport properties of $LiNbO_3$ and $LiTaO_3$ requires further studies of oxygen and cation diffusion as well as of different defect types at elevated temperatures. Although the first steps toward this correlation have been performed, such complex investigations are beyond the scope of the current work and will be performed in subsequent research.

4. Conclusions

In order to examinate the general assumption that LN and LT crystals are to a great extent alike, and understand how far the knowledge collected in the last decades on LN is generally valid, we have performed a parallel investigation of polaronic structures, optical response and electrical conductivity of LN and LT.

First principles calculations reveal the existence of point defects in LT compatible with the polaronic picture established in LN. Structures compatible with our knowledge of free polarons (Ta_{Ta}^{4+}), small bound polarons (Ta_{Li}^{4+}) and bipolarons ($Ta_{Li}^{4+} - Ta_{Ta}^{4+}$) have been modeled. They are characterized by a major rearrangement of the atomic structure and, in the case of bipolarons, by the formation of a covalent bond between Ta atoms. The charge distribution analysis confirms the localized nature of the polaronic states, which can thus be addressed as small polarons. Although polaronic defects in LN behave similarly to their counterpart in LT, differences in the electronic structure suggest differences in the optical response and in charge transport.

Due to the comparable electronic structure and to the occurrence of similar polaronic defects, the appearance of transient absorption and transient luminescence as optical phenomena in LT can be expected. With respect to the kinetics, qualitative similar behaviors in LN and LT are expected. Experimentally, it is widely established for LN that the presence of small polarons bound to a Nb_{Li} antisite defect center, to regular Nb_{Nb} sites or of $Nb_{Nb}^{4+} - Nb_{Li}^{4+}$ bipolarons results in pronounced optical fingerprints in the visible and near-infrared spectrum. Time-resolved spectroscopy studies performed in the present work additionally enable to clearly validate small polaron formation and hopping transport. The observation of a transient absorption in LT crystals upon single pulse exposure thus represents a sufficient condition to assume the presence of polarons with strong coupling to the lattice in LT, as predicted by theory. Remarkably, the signal appears in a spectral region ($\lambda = 910$ nm) that is quite similar to the Nb_{Li} small polaron in LN, so that electrons coupled to Ta_{Li} antisite defect centers might be reasonably assumed at its origin. A much more striking finding is the observation of a rise time of the transient absorption upon the laser pulse, that is a characteristic feature of small polaron formation. From the comparison of transient absorption and transient luminescence between LT and LN, we find that the transient absorption features much longer relaxation lifetimes together with a simplified decay path. LT here resembles rather a Mg doped LN sample than a congruent one including a large density of antisite defects. At the same time, transient luminescence appears with striking similarity in the sub-ps to ps time regime in both crystals. Considering both findings, we can conclude that the defect alterations strongly affect the small polaron hopping while the 3D lattice structure does not influence the macroscopic features.

Electrical conductivity measurements in air in the temperature range from about 350 °C to 920 °C demonstrate similar activation energies and magnitudes of electrical conductivity for LN and LT samples below 600 °C, thereby indicating closely related conduction mechanisms. As the dominating transport mechanism in LN is due to Li transport via Li vacancies, it is plausible to assume that also in LT this transport channel plays a major role. This is in turn in agreement with the *ab initio* calculations, which predict the spontaneous formation of Li vacancies, which are exotherm for a wide range of Fermi energy values within the LT fundamental gap. Above 600 °C the electrical conductivity of LT and LN differs. For example, LN shows a gradually increasing slope $E_{\sigma T}$ with temperature which indicates a transition range with contributions of two or more conduction mechanisms. For our data, the activation energy cannot be

easily determined, as the slope is not constant and the underlying conductivity mechanisms are not yet known. Detailed investigations of the high-temperature conductivity are subject to subsequent studies.

The results suggest that the knowledge of the physical mechanisms gathered on LN can be transferred to some extent to other ferroelectric oxides such as LT and related solid solutions. However Curie and melt temperature in LN and LT are very different. Thus, solid solutions of the two materials will offer the possibility to exploit and tune the temperature dependence of many materials properties. This makes $LiNb_{1-x}Ta_xO_3$ solid solutions a promising and exciting field of research for the near future.

Acknowledgments

The Deutsche Forschungsgemeinschaft (DFG) is gratefully acknowledged for financial support via projects FOR5044, (SA 1948/2-1), IM37/11-1, FR1301/32-1 and INST 190/165-1 FUGG. Calculations for this research were conducted on the Lichtenberg high performance computer of the TU Darmstadt as well as at the Höchstleistungrechenzentrum Stuttgart (HLRS). We further acknowledge computational resources provided by the HPC Core Facility and the HRZ of the Justus-Liebig-Universität Gießen. Dr L Kovács and coworkers from the WIGNER Research Center for Physics, Budapest, Dr. D Roshchupkin and Dr B Red'kin from the Institute of Microelectronics Technology and High Purity Materials, Russian Academy of Sciences, Moscow, are thankfully acknowledged for providing the congruent $LiNbO_3$ sample used for optical and electrical measurements respectively.

Data availability statement

All data that support the findings of this study are included within the article (and any supplementary files).

ORCID iDs

A Krampf https://orcid.org/0000-0001-5790-9379
S Sanna https://orcid.org/0000-0003-4416-0252

References

[1] Matthias B T and Remeika J P 1949 Ferroelectricity in the ilmenite structure *Phys. Rev.* **76** 1886–7
[2] Lee T-C, Lee J-T, Robert M A, Wang S and Rabson T A 2003 Surface acoustic wave applications of lithium niobate thin films *Appl. Phys. Lett.* **82** 191–3
[3] Räuber A 1978 *Chemistry and Physics of Lithium Niobate* (*Current Topics in Materials Science* vol 1) (Amsterdam: Elsevier)
[4] Stone G, Knorr B, Gopalan V and Dierolf V 2011 Frequency shift of Raman modes due to an applied electric field and domain inversion in $LiNbO_3$ *Phys. Rev.* B **84** 134303
[5] Fontana M D and Bourson P 2015 Microstructure and defects probed by Raman spectroscopy in lithium niobate crystals and devices *Appl. Phys. Rev.* **2** 040602
[6] Jungk T, Hoffmann Á and Soergel E 2006 Detection mechanism for ferroelectric domain boundaries with lateral force microscopy *Appl. Phys. Lett.* **89** 042901
[7] Johann F and Soergel E 2009 Quantitative measurement of the surface charge density *Appl. Phys. Lett.* **95** 232906
[8] Luedtke F, Buse K and Sturman B 2012 Hidden reservoir of photoactive electrons in $LiNbO_3$ crystals *Phys. Rev. Lett.* **109** 026603
[9] Margueron S, Bartasyte A, Glazer A M, Simon E, Hlinka J, Gregora I and Gleize J 2012 Resolved E-symmetry zone-centre phonons in $LiTaO_3$ and $LiNbO_3$ *J. Appl. Phys.* **111** 104105
[10] Bartasyte A *et al* 2009 Residual stress estimation in ferroelectric $PbTiO_3$ thin films by Raman spectroscopy *Phys. Rev.* B **79** 104104
[11] Ridah A, Fontana M D and Bourson P 1997 Temperature dependence of the Raman modes in $LiNbO_3$ and mechanism of the phase transition *Phys. Rev.* B **56** 5967–73
[12] Zelenovskiy P S, Shur V Y, Bourson P, Fontana M D, Kuznetsov D K and Mingaliev E A 2010 Raman study of neutral and charged domain walls in lithium niobate *Ferroelectrics* **398** 34–41
[13] Fontana M D, Hammoum R, Bourson P, Margueron S and Shur V Y 2008 Raman probe on PPLN microstructures *Ferroelectrics* **373** 26–31
[14] Araujo R M, Lengyel K, Jackson R A, Kovács L and Valerio M E G 2007 A computational study of intrinsic and extrinsic defects in $LiNbO_3$ *J. Phys.: Condens. Matter.* **19** 046211
[15] Araujo R M, Valerio M E G and Jackson R A 2014 Computer simulation of metal co-doping in lithium niobate *Proc. R. Soc.* A **470** 20140406
[16] Schirmer O F, Imlau M, Merschjann C and Schoke B 2009 Electron small polarons and bipolarons in $LiNbO_3$ *J. Phys.: Condens. Matter.* **21** 123201
[17] Schirmer O F, Imlau M and Merschjann C 2011 Bulk photovoltaic effect of $LiNbO_3$:Fe and its small-polaron-based microscopic interpretation *Phys. Rev.* B **83** 165106
[18] Donnerberg H, Tomlinson S M, Catlow C R A and Schirmer O F 1991 Computer-simulation studies of intrinsic defects in $LiNbO_3$ crystals *Phys. Rev.* B **44** 4877–83

[19] Abdi F, Fontana M D, Aillerie M and Bourson P 2006 Coexistence of Li and Nb vacancies in the defect structure of pure $LiNbO_3$ and its relationship to optical properties *Appl. Phys.* A **83** 427–34
[20] Abrahams S C and Marsh P 1986 Defect structure dependence on composition in lithium niobate *Acta Crystallogr.* B **42** 61–8
[21] Iyi N, Kitamura K, Izumi F, Yamamoto J K, Hayashi T, Asano H and Kimura S 1992 Comparative study of defect structures in lithium niobate with different compositions *J. Solid State Chem.* **101** 340–52
[22] Schirmer O F, Thiemann O and Wöhlecke M 1991 Defects in $LiNbO_3$—I. experimental aspects *J. Phys. Chem. Solids* **52** 185–200
[23] Mouras R, Fontana M D, Bourson P and Postnikov A V 2000 Lattice site of Mg ion in $LiNbO_3$ crystal determined by Raman spectroscopy *J. Phys.: Condens. Matter.* **12** 5053–9
[24] Quispe-Siccha R *et al* 2009 The effect of Nd and Mg doping on the micro-Raman spectra of $LiNbO_3$ single-crystals *J. Phys.: Condens. Matter.* **21** 145401
[25] Gopalan V, Dierolf V and Scrymgeour D A 2007 Defect-domain wall interactions in trigonal ferroelectrics *Annu. Rev. Mater. Res.* **37** 449–89
[26] Falk M, Japs J, Woike T and Buse K 2007 Charge transport in highly iron-doped oxidized lithium niobate single crystals *Appl. Phys.* B **87** 119–22
[27] Vitova T, Hormes J, Falk M and Buse K 2009 Holographic data storage technology *J. Appl. Phys.* **105** 013524
[28] Buse K, Adibi A and Psaltis D 1998 Non-volatile holographic storage in doubly doped lithium niobate crystals *Nature* **393** 665–8
[29] Fritze H, Schulz M, Seh H and Tuller H L 2004 High temperature operation and stability of langasite resonators *MRS Online Proc. Libr.* **828** A3.9/K4.9
[30] Fritze H and Tuller H L 2002 High-temperature balance *US Patent No.* 6.370.955
[31] Weidenfelder A, Shi J, Fielitz P, Borchardt G, Becker K D and Fritze H 2012 Electrical and electromechanical properties of stoichiometric lithium niobate at high-temperatures *Solid State Ion.* **225** 26–9
[32] Weidenfelder A, Fritze H, Fielitz P, Borchardt G, Shi J, Becker K-D and Ganschow S 2012 Transport and electromechanical properties of stoichiometric lithium niobate at high temperatures *Phys. Chem.* **226** 421–9
[33] Fielitz P, Schneider O, Borchardt G, Weidenfelder A, Fritze H, Shi J, Becker K D, Ganschow S and Bertram R 2011 Oxygen-18 tracer diffusion in nearly stoichiometric single crystalline lithium niobate *Solid State Ion.* **189** 1–6
[34] Gervais F and Fonseca V 1997 Lithium tantalate ($LiTaO_3$) *Handbook of Optical Constants of Solids* ed E D Palik (New York: Academic) pp 777–805
[35] Shur V Y 2010 Lithium niobate and lithium tantalate-based piezoelectric materials *Advanced Piezoelectric Materials: Science and Technology* (Sawston: Woodhead Publishing) pp 204–38
[36] Wong K K 2002 *Properties of Lithium Niobate* (*EMIS Datareviews Series*) (London: INSPEC/Institution of Electrical Engineers)
[37] Bentini G G *et al* 2005 Structural and compositional characterization of X-cut $LiNbO_3$ crystals implanted with high energy oxygen and carbon ions *Nucl. Instrum. Methods Phys. Res.* **240** 174–7
[38] Sanna S and Schmidt W G 2010 Lithium niobate X-cut, Y-cut, and Z-cut surfaces from *ab initio* theory *Phys. Rev.* B **81** 214116
[39] Rode S, Hölscher R, Sanna S, Klassen S, Kobayashi K, Yamada H, Schmidt W G and Kühnle A 2012 Atomic-resolution imaging of the polar $(000\bar{1})$ surface of $LiNbO_3$ in aqueous solution by frequency modulation atomic force microscopy *Phys. Rev.* B **86** 075468
[40] Weis R S and Gaylord T K 1985 Lithium niobate: summary of physical properties and crystal structure *Appl. Phys.* A **37** 191–203
[41] Volk T and Wöhlecke M 2009 *Lithium Niobate, Defects, Photorefraction and Ferroelectric Switching* (*Springer Series in Materials Science* vol 115) (Berlin: Springer)
[42] Friedrich M, Schindlmayr A, Schmidt W G and Sanna S 2016 $LiTaO_3$ phonon dispersion and ferroelectric transition calculated from first principles *Phys. Status Solidi (b)* **253** 683–9
[43] Korth kristalle gmbh https://www.korth.de/index.php/startseite-124.html
[44] Kim S, Gopalan V and Gruverman A 2002 Coercive fields in ferroelectrics: a case study in lithium niobate and lithium tantalate *Appl. Phys. Lett.* **80** 2740–2
[45] He W, Gao X, Pang L, Wang D, Gao N and Wang Z 2016 First-principles investigation of vacancies in $LiTaO_3$ *J. Phys.: Condens. Matter.* **28** 315501
[46] Vyalikh A *et al* 2018 Analysis of the defect clusters in congruent lithium tantalate *Phys. Rev. Mater.* **2** 013804
[47] Krampf A, Messerschmidt S and Imlau M 2020 Superposed picosecond luminescence kinetics in lithium niobate revealed by means of broadband fs-fluorescence upconversion spectroscopy *Sci. Rep.* **10** 11397
[48] Kresse G and Furthmüller J 1996 Efficiency of *ab-initio* total energy calculations for metals and semiconductors using a plane-wave basis set *Comput. Mater. Sci.* **6** 15–50
[49] Kresse G and Furthmüller J 1996 Efficient iterative schemes for *ab initio* total-energy calculations using a plane-wave basis set *Phys. Rev.* B **54** 11169
[50] Kresse G and Joubert D 1999 From ultrasoft pseudopotentials to the projector augmented-wave method *Phys. Rev.* B **59** 1758–75
[51] Blöchl P E 1994 Projector augmented-wave method *Phys. Rev.* B **50** 17953–79
[52] Sanson A, Zaltron A, Argiolas N, Sada C, Bazzan M, Schmidt W G and Sanna S 2015 Polaronic deformation at the $Fe^{2+/3+}$ impurity site in Fe : $LiNbO_3$ crystals *Phys. Rev.* B **91** 094109
[53] Perdew J P, Burke K and Ernzerhof M 1996 Generalized gradient approximation made simple *Phys. Rev. Lett.* **77** 3865–8
[54] Monkhorst H J and Pack J D 1976 Special points for Brillouin-zone integrations *Phys. Rev.* B **13** 5188–92
[55] Anisimov V I, Aryasetiawan F and Lichtenstein A I 1997 First-principles calculations of the electronic structure and spectra of strongly correlated systems: the LDA + U method *J. Phys.: Condens. Matter.* **9** 767–808
[56] Dudarev S L, Botton G A, Savrasov S Y, Humphreys C J and Sutton A P 1998 Electron-energy-loss spectra and the structural stability of nickel oxide: an LSDA + U study *Phys. Rev.* B **57** 1505–9
[57] Winter M 2021 THE periodic table on the WWW www.webelements.com (Accessed: 15 February 2021)
[58] Sanna S, Hourahine B, Gerstmann U and Frauenheim T 2007 Efficient tight-binding approach for the study of strongly correlated systems *Phys. Rev.* B **76** 155128
[59] Solovyev I V, Dederichs P H and Anisimov V I 1994 Corrected atomic limit in the local-density approximation and the electronic structure of *d* impurities in Rb *Phys. Rev.* B **50** 16861–71
[60] Sanna S, Neufeld S, Rüsing M, Berth G, Zrenner A and Schmidt W G 2015 Raman scattering efficiency in $LiTaO_3$ and $LiNbO_3$ crystals *Phys. Rev.* B **91** 224302
[61] Rüsing M *et al* 2018 Imaging of 180° ferroelectric domain walls in uniaxial ferroelectrics by confocal Raman spectroscopy: unraveling the contrast mechanism *Phys. Rev. Mater.* **2** 103801
[62] Nahm H H and Park C H 2008 First-principles study of microscopic properties of the Nb antisite in $LiNbO_3$: comparison to phenomenological polaron theory *Phys. Rev.* B **78** 184108

[63] Friedrich M, Schmidt W G, Schindlmayr A and Sanna S 2017 Optical properties of titanium-doped lithium niobate from time-dependent density-functional theory *Phys. Rev. Mater.* **1** 034401
[64] Friedrich M, Schmidt W G, Schindlmayr A and Sanna S 2017 Polaron optical absorption in congruent lithium niobate from time-dependent density-functional theory *Phys. Rev. Mater.* **1** 054406
[65] Gerecke M, Bierhance G, Gutmann M, Ernsting N P and Rosspeintner A 2016 Femtosecond broadband fluorescence upconversion spectroscopy: spectral coverage versus efficiency *Rev. Sci. Instrum.* **87** 053115
[66] Qiu Y, Ucer K B and Williams R T 2005 Formation time of a small electron polaron in $LiNbO_3$: measurements and interpretation *Phys. Status Solidi (c)* **2** 232–5
[67] Sasamoto S, Hirohashi J and Ashihara S 2009 Polaron dynamics in lithium niobate upon femtosecond pulse irradiation: influence of magnesium doping and stoichiometry control *J. Appl. Phys.* **105** 083102
[68] Freytag F, Booker P, Corradi G, Messerschmidt S, Krampf A and Imlau M 2018 Picosecond near-to-mid-infrared absorption of pulse-injected small polarons in magnesium doped lithium niobate *Opt. Mater. Express* **8** 1505–14
[69] Xu H, Lee D, He J, Sinnott S B, Gopalan V, Dierolf V and Phillpot S R 2008 Stability of intrinsic defects and defect clusters in $LiNbO_3$ from density functional theory calculations *Phys. Rev.* B **78** 174103
[70] Li Y, Schmidt W G and Sanna S 2014 Intrinsic $LiNbO_3$ point defects from hybrid density functional calculations *Phys. Rev.* B **89** 094111
[71] Li Y, Sanna S and Schmidt W G 2014 Modeling intrinsic defects in $LiNbO_3$ within the Slater–Janak transition state model *J. Chem. Phys.* **140** 234113
[72] Xu H, Chernatynskiy A, Lee D, Sinnott S B, Gopalan V, Dierolf V and Phillpot S R 2010 Stability and charge transfer levels of extrinsic defects in $LiNbO_3$ *Phys. Rev.* B **82** 184109
[73] Li Q, Wang B, Woo C H, Wang H and Wang R 2007 First-principles study on the formation energies of intrinsic defects in $LiNbO_3$ *J. Phys. Chem. Solids* **68** 1336–40
[74] Kappers L A, Sweeney K L, Halliburton L E and Liaw J H W 1985 Oxygen vacancies in lithium tantalate *Phys. Rev.* B **31** 6792–4
[75] Beyer O, Maxein D, Buse K, Sturman B, Hsieh H T and Psaltis D 2005 Investigation of nonlinear absorption processes with femtosecond light pulses in lithium niobate crystals *Phys. Rev.* E **71** 056603
[76] Beyer O, Maxein D, Woike T and Buse K 2006 Generation of small bound polarons in lithium niobate crystals on the subpicosecond time scale *Appl. Phys.* B **83** 527–30
[77] Yamada Y and Kanemitsu Y 2013 Photoluminescence spectra of perovskite oxide semiconductors *J. Lumin.* **133** 30–4
[78] Krol D M, Blasse G and Powell R C 1980 The influence of the Li/Nb ratio on the luminescence properties of $LiNbO_3$ *J. Chem. Phys.* **73** 163–6
[79] Messerschmidt S, Krampf A, Freytag F, Imlau M, Vittadello L, Bazzan M and Corradi G 2019 The role of self-trapped excitons in polaronic recombination processes in lithium niobate *J. Phys.: Condens. Matter.* **31** 065701
[80] Corradi G, Krampf A, Messerschmidt S, Vittadello L and Imlau M 2020 Excitonic hopping-pinning scenarios in lithium niobate based on atomistic models: different kinds of stretched exponential kinetics in the same system *J. Phys.: Condens. Matter.* **32** 413005
[81] Yusupov R V, Gracheva I N, Rodionov A A, Syrnikov P P, Gubaev A I, Dejneka A, Jastrabik L, Trepakov V A and Salakhov M K 2011 Experimental manifestations of the Nb^{4+}–O^- polaronic excitons in $KTa_{0.988}Nb_{0.012}O_3$ *Phys. Rev.* B **84** 174118
[82] Eglitis R I, Kotomin E A and Borstel G 2002 Quantum chemical modelling of 'green' luminescence in ABO perovskites *Eur. Phys. J.* B **27** 483–6
[83] Kotomin E A, Eglitis R I and Borstel G 2000 Quantum chemical modelling of electron polarons and excitons in ABO_3 perovskites *J. Phys.: Condens. Matter.* **12** L557–62
[84] Huanosta A and West A R 1987 The electrical properties of ferroelectric $LiTaO_3$ and its solid solutions *J. Appl. Phys.* **61** 5386–91